Conservation of the structural and functional architecture of encapsulated ferritins in bacteria and archaea

Conservation of the structural and functional architecture of encapsulated ferritins in bacteria and archaea

Didi He[1,#,♣], Cecilia Piergentili[2,♣], Jennifer Ross[3,♣], Emma Tarrant[4], Laura R. Tuck[1], C. Logan Mackay[3], Zak McIver[2], Kevin J. Waldron[4], David J. Clarke[3*], Jon Marles-Wright[2*],

[1]Institute of Quantitative Biology, Biochemistry and Biotechnology, School of Biological Sciences, The University of Edinburgh, Max Born Crescent, Edinburgh, EH9 3BF; [2]School of Natural and Environmental Sciences, Newcastle University. Newcastle upon Tyne, NE1 7RU; [3]EaStCHEM School of Chemistry, The University of Edinburgh, Joseph Black Building, David Brewster Road, Edinburgh, Scotland, EH9 3FJ; [4]Institute for Cell and Molecular Biosciences, Newcastle University, Newcastle upon Tyne, NE2 4HH.

[#]*Current address: Structural Genomics Consortium, University of Oxford, Old Road Campus Research Building, Roosvelt Drive, Oxford, OX3 7DQ*

Running title: Structure and function of EncFtn homologues

♣ These authors contributed equally to this work

* To whom correspondence should be addressed:

Jon Marles-Wright, +44(0)191 208 4855, Jon.marles-wright1@ncl.ac.uk;

David J. Clarke, +44(0)131 650 4808, Dave.clarke@ed.ac.uk.

KEYWORDS: encapsulin, encapsulated ferritin, ferritin, ferroxidase, mass spectrometry (MS), metalloprotein, protein assembly, Pyrococcus furiosus, Haliangium ochraceum, X-ray crystallography

Abstract

Ferritins are a large family of intracellular proteins that protect the cell from oxidative stress by catalytically converting Fe(II) into less toxic Fe(III) and storing iron minerals within their core. Encapsulated ferritins (EncFtn) are a sub-family of ferritin-like proteins, which are widely distributed in all bacterial and archaeal phyla. The recently characterized *Rhodospirillum rubrum* EncFtn displays an unusual structure when compared to classical ferritins, with an open decameric structure that is enzymatically active, but unable to store iron. This EncFtn must be associated with an encapsulin nanocage in order to act as an iron store. Given the wide distribution of the EncFtn family in organisms with diverse environmental niches, a question arises as to whether this unusual structure is conserved across the family. Here, we characterize EncFtn proteins from the halophile *Haliangium ochraceum* and the thermophile *Pyrococcus furiosus*, which show the conserved annular pentamer of dimers topology. Key structural differences are apparent between the homologues, particularly in the centre of the ring and the secondary metal binding site, which is not conserved across the homologues. Solution and native mass spectrometry analyses highlight that the stability of the protein quaternary structure differs between EncFtn proteins from different species. The ferroxidase activity of EncFtn proteins was confirmed, and we show that while the quaternary structure around the ferroxidase centre is distinct to classical ferritins, the ferroxidase activity is still inhibited by Zn(II). Our results highlight the common structural organization and activity of EncFtn proteins, despite diverse host environments and contexts within encapsulins.

Introduction

The encapsulated ferritins (**EncFtn**) are recently described members of the ferritin superfamily [1–3]. These proteins are sequestered within encapsulin nanocompartments, and the two proteins act in concert to provide an iron storage system with a much greater capacity than the classical ferritins and DNA-binding Protein from Starved cells (DPS) nanocages [3,4]. Genes encoding encapsulin-associated ferritins have been identified in a wide range of bacterial and archaeal species that inhabit diverse ecological niches from ponds, streams (*Rhodospirillum rubrum)*, and coastal seas (*Haliangium ochraceum*), to abyssal ocean vents (*Pyrococcus furiosus)* [5].

The *R. rubrum* EncFtn was the first protein in its family to be structurally and biochemically characterized; it has a fold with two antiparallel alpha-helices that adopts an annular-decamer quaternary structure, assembled as a pentamer of dimers [1]. The subunits dimerize through metal-mediated contacts to reconstitute the four-helix ferritin fold with a functional ferroxidase centre [6,7]. While the EncFtn protein displays ferroxidase activity, it is not capable of storing iron in the same way as other ferritins due to its open architecture and the lack of an enclosed cavity for iron mineralization [8,9]; therefore, EncFtn family proteins must be localized to the interior of an encapsulin nanocage for efficient iron storage [1,3,5]. Localization to encapsulin nanocages is mediated by a short encapsulation sequence, which is usually appended to the C-terminus of the EncFtn protein chain [1,3,5,10]; addition of this sequence to heterologous proteins is sufficient to direct them to the lumen of encapsulins [11,12].

The encapsulin protein family is structurally related to the HK97 bacteriophage shell protein and they form icosahedral nanocages of between 25 and 35 nm in diameter. Pores are formed at the icosahedral symmetry axes between subunits to allow substrate access to encapsulated enzyme cargoes [3,5,10,13]. The *R. rubrum* encapsulin was shown to associate with over 2000 iron ions per capsid, while being catalytically inactive; and, in concert with EncFtn, capable of mineralizing and storing more than four times as much iron as a classical ferritin nanocage [1]. Given the wide distribution of encapsulin proteins across bacterial and archaeal phyla, and the conservation of the EncFtn proteins in 20 % of all phyla with encapsulin genes, we investigated the structure and activity of EncFtn proteins from the halophilic Proteobacterium *H. ochraceum* and the EncFtn-fusion from

the Euryarchaeota *P. furiosus*, to determine whether the structural and functional organization seen in the *R. rubrum* EncFtn is conserved within its phylum and between domains and environmental niches.

Here we report the structural and biochemical characterization of members of the EncFtn family from *H. ochraceum* and *P. furiosus*. Both proteins adopt similar topology to the *R. rubrum* EncFtn and assemble as annular decamers formed from pentamers of dimers, with ferroxidase centres located at one of the dimer interfaces. The ferroxidase activities of the proteins are comparable, and they show similar levels of inhibition by the competing metal ion zinc. These data show that the structural and biochemical features of encapsulated ferritins are conserved across different environmental niches and phyla with particular adaptations for thermal stability in thermophilic microorganisms.

Materials and Methods

Cloning expression and purification of EncFtn and EncFtn homologues

Recombinant encapsulated ferritin from *Rhodospirillum rubrum* was produced as described previously [1]. DNA fragments encoding truncated versions of the encapsulated ferritins from *Haliangium ochraceum* (Hoch_$3836_{1\text{-}98}$) (Uniprot: D0LZ73_HALO1) and *Pyrococcus furiosus* (Pfc_$01575_{1\text{-}99}$) (Uniprot: I6U7J4_9EURY) were produced as double-stranded gBlocks (IDT) and codon optimized for expression in *E. coli*, with restriction endonuclease sites for insertion into pET-28a (Pfc_$05157_{1\text{-}99}$) or a modified pET-28 vector with CIDAR MoClo [14] Golden Gate cloning sites (Hoch_$3836_{1\text{-}98}$). Untagged and His-tagged variants were produced for both proteins in this way. A StrepII-tagged variant of each protein was produced by assembly of the EncFtn gBlock into a CIDAR MoClo destination vector with a custom T7 promoter and StrepII-tag terminator part. Sequences of primers and gBlocks used in this study are shown in Tables S1 and S2 respectively, and the sequences of expressed proteins are shown in Table S3. The expression plasmids were transformed into *E. coli* BL21(DE3) cells and a single colony was grown overnight at 37 °C in 100 ml LB medium, supplemented with 35 μg/ml kanamycin, with shaking at 180 rpm. The cells were sub-cultured into 1 L of LB or M9 minimal medium, grown until OD_{600}=0.6, and protein production was induced with 1 mM IPTG, the temperature was reduced to 18 °C and cells were incubated for a further 18 hours.

Cells were harvested by centrifugation at 4,000 × *g* and washed with PBS. Cell-free extract was produced by resuspending cells in 10 x v/w Buffer A (50 mM Tris-HCl, pH 8.0) and sonicated on ice for 5 minutes with 30 s on/off cycle at 60 watts power output. The lysate was cleared by centrifugation at 35,000 × *g* and filtered with a 0.45 μm syringe filter. Untagged recombinant proteins were purified from cell-free extract by anion exchange using HiPrep Q sepharose fast-flow 16/10 column (GE Healthcare) equilibrated with Buffer A. Cell free extract was applied to the column and unbound proteins were washed off with 10 column volumes of Buffer A. Proteins were eluted with a linear gradient of Buffer B (50 mM Tris-HCl, pH 8.0, 1 M NaCl) over 20 column volumes and fractions collected.

His-tagged proteins were purified by resuspending cells in 10 x (v/w) Buffer HisA (50 mM Tris-HCl, pH 8.0, 500 mM NaCl, 50 mM imidazole) before sonication and clarification as above. Clarified cell

lysate was applied to a 5 ml HisTrap FF column (GE Healthcare) and unbound proteins were washed off with 10 column volumes of Buffer HisA. A step-gradient of 50 % and 100 % Buffer HisB (50 mM Tris-HCl, pH 8.0, 500 mM NaCl, 500 mM imidazole) was used to elute His-tagged proteins.

Fractions of Q sepharose or His-trap eluent containing the protein of interest, as identified by 15 % (w/v) SDS-PAGE, were subjected to size-exclusion chromatography using an S200 16/60 column, previously calibrated with LMW/HMW calibration kits (GE Healthcare) (Fig. S1) and equilibrated with Buffer GF (50 mM Tris-HCl, pH 8.0, 150 mM NaCl).

StrepII-tagged proteins were purified by suspending cells in 10 x (v/w) Buffer W (100 mM Tris pH 8.0, 150 mM NaCl) before sonication and clarification as described above. Cell lysate was applied to Strep-Trap HP column (GE Healthcare), prepared as suggested by the manufacturer, and unbound proteins were washed off by applying 5 column volumes of Buffer W. Strep-tagged proteins were eluted by Buffer E (100 mM Tris pH 8.0, 150 mM NaCl, 2.5 mM desthiobiotin). Eluted protein was buffer-exchanged to Buffer GF by centrifugal concentrator Vivaspin Turbo (Sartorius, 10 kDa MWCO) to remove desthiobiotin.

Protein quantification

Purified protein concentration was determined by colorimetric technique using the Pierce™ BCA protein assay kit following manufacturer specifications for the standard Test-tube procedure at 37 °C. Diluted bovine serum albumin (BSA) standards were prepared in GF buffer. Fig. S2*A*/*B* show colour response curves prepared for His-tagged or Strep-tagged protein quantification, respectively. Protein samples absorbance at 562 nm (average of 3 experimental replicates) are listed in Table S4.

Ferroxidase assays

Ferroxidase activity of the enzymes was tested by following the formation of Fe(III) species by UV-visible spectroscopy at 20 °C, as previously described [1]. Oxygen-free aliquots of Fe(II) (1 mM) were prepared by dissolving $FeSO_4.7H_2O$ in 0.1 % (v/v) HCl under anaerobic conditions. Purified proteins (decameric fraction) were diluted anaerobically to the final concentration of 10 μM monomer in Buffer H (10 mM HEPES pH 8.0, 150 mM NaCl). Protein and Fe(II) samples were added to a

quartz cuvette (Hellma) under aerobic conditions at the final concentration of 10 and 50 μM, respectively. Absorbance at 315 nm was monitored every second over 1500 s using a UV-visible spectrophotometer (Perkin Elmer Lambda 35) using the provided TimeDrive software. A negative control was performed by monitoring the progress curve at A_{315} of Fe(II) salt sample in the absence of protein. Data presented here are the mean of three technical replicates of time zero-subtracted progress curves with standard deviations calculated from the mean.

Zinc inhibition of ferroxidase activity

In order to test enzyme selectivity toward Fe(II), the ferroxidase assay was carried out as previously described [1], in the presence of $FeSO_4.7H_2O$ (50 μM) and various concentrations of $ZnSO_4.2H_2O$. The A_{315} nm progress curve of protein mixed with the highest concentration of Zn(II) used in the assay (100 μM) was also monitored as a negative control.

Protein Crystallography

Hoch_EncFtn and Pfc_EncFtn were concentrated to 10 mg/ml using a 10 kDa MWCO centrifugal concentrator (Vivaspin) and subjected to sitting drop vapor diffusion crystallization using 70 μl well solution and drops of 100 nl protein, plus 100 nl well solution. Crystals of Hoch_EncFtn grew in well solution containing 0.2 M NaCl, 0.1 M Bis-Tris, pH 5.5, 20 % (w/v) PEG 3350; and crystals of Pfc_EncFtn were found in a condition containing 0.2 M $LiSO_4.H_2O$, 20 % (w/v) PEG 3350. Crystals were harvested using a LithoLoop (Molecular Dimensions Limited), transferred to a cryoprotection solution of well solution supplemented with 20 % (v/v) PEG 200 and flash cooled in liquid nitrogen. Diffraction data were collected at Diamond Light Source at 100 K using a Pilatus 6M detector. Images were integrated and scaled using XDS [15]; the correct crystallographic symmetry group was confirmed with Pointless [16] and reflections were merged with Aimless [17]. The data were phased by molecular placement using Phaser, with a decamer of Rru_EncFtn (PDB ID: 5DA5) used as the search model [1]. This has 58 and 22 % sequence identity to the Hoch_EncFtn and Pfc_EncFtn respectively. The sequences were aligned with the 5DA5 protein sequence using ClustalOmega and the alignment was used to edit the search model to match the target sequence using CHAINSAW [18]. The crystallographic models were rebuilt using phenix.autobuild [19] and subsequently refined

using phenix.refine [20] with cycles of manual model building in Coot [21]. The model quality was assessed using MolProbity [22]. All structural figures were generated using PyMOL (www.pymol.org). X-ray data collection and refinement statistics are shown in Table 1.

Sequence alignment and depiction

The protein sequences for Hoch_3836 and the encapsulated ferritin domain of Pfc_05175 were aligned against Rru_A0973 using Clustal Omega [23] and rendered using ESPript 3.0 [24].

Mass spectrometry

All mass spectrometry (MS) experiments were performed on a Synapt G2 ion-mobility equipped Q-ToF instrument (Waters Corp., Manchester, UK). LC-MS experiments were performed using an Acquity UPLC equipped with a reverse phase C4 Aeris Widepore 50 × 2.1 mm HPLC column (Phenomenex, CA, USA) and a gradient of 5–95% acetonitrile (0.1% formic acid) over 10 minutes was employed. For LC-MS, samples were typically analysed at 5 μM, and data analysis was performed using MassLynx v4.1 and MaxEnt deconvolution. For native MS analysis, all protein samples were buffer exchanged into 100 mM ammonium acetate (pH 8.0, or pH 5.0) using Micro Biospin Chromatography Columns (Bio-Rad, UK) prior to analysis and the resulting protein samples were analysed at a typical final concentration of ~5 μM (oligomer concentration). For native MS ionization, nano-ESI was employed using a nanomate nanoelectrospray infusion robot (Advion Biosciences, Ithaca, NY). Instrument parameters were tuned to preserve non-covalent protein complexes and were consistent for the analysis of all protein homologues. After the native MS optimization, parameters were: nanoelectrospray voltage 1.60 kV; sample cone 100 V; extractor cone 0 V; trap collision voltage 4 V; source temperature 60 °C; and source backing pressure 6.0 mbar.

ICP-MS

Inductively coupled plasma mass spectrometry experiments were performed on samples of Rru_His, Hoch_His, and Pfc_His from size-exclusion chromatography experiments and Rru_StrepII, Hoch_StrepII, and Pfc_StrepII from the affinity chromatography purification step as described previously [1].

Results

Purification of encapsulated ferritins from H. ochraceum and P. furiosus

The encapsulated ferritins from *H. ochraceum* and *P. furiosus* share 18 % amino acid sequence identity with each other, and 58 % and 22 % with the *R. rubrum* EncFtn (respectively referred to as Hoch_EncFtn, Pfc_EncFtn, and Rru_EncFtn herein). Residues shown to be in the ferroxidase centre of the Rru_EncFtn protein are strictly conserved in the Hoch_EncFtn and Pfc_EncFtn proteins, with secondary metal binding sites conserved in Hoch_EncFtn, but not in Pfc_EncFtn (Fig. S3).

To explore the structure and function of encapsulated ferritins from different species, we produced examples of this protein family from *H. ochraceum* and *P. furiosus* as truncated variants, lacking the C-terminal encapsulin localization sequence, by heterologous expression in *Escherichia coli*. The *H. ochraceum* EncFtn was produced as a C-terminal His-tagged variant, C-terminal StrepII-tagged variant, and an untagged variant comprising residues 1-98 of the native polypeptide. In *P. furiosus* the encapsulated ferritin forms a single contiguous polypeptide with the encapsulin shell protein; therefore, a truncated version with residues 1-99 encompassing just the EncFtn domain was produced as both a C-terminal His-tagged variant, a C-terminal StrepII-tagged variant, and an untagged variant. Purity and yield issues with untagged proteins were behind the rational of using tagged-variants. His-tagged variants were produced for mass-spectrometry analysis, whereas C-terminal StrepII-tagged variants were used in the enzymatic assay where the presence of the His-tag could have interfered with metal binding and catalysis. Native untagged proteins were used for protein crystallography as, after several attempts, only these variants produced crystals suitable for X-ray diffraction. Average neutral masses were obtained for each homologue by liquid chromatography mass spectrometry (Table S5). These all agree with the predicted masses of each protein and revealed that some of the variants lacked full processing of the initiating methionine.

To interrogate the behaviour of the EncFtn homologues in solution, both the His-tagged and StrepII-tagged variants were subjected to S200 size-exclusion chromatography, calibrated with standards of known molecular weight, and followed by SDS-PAGE analysis (Fig. 1, Table S6, and Fig. S4). Hoch_His eluted as three peaks of increasing area: a small peak at ~70 ml consistent with a decamer

oligomer; a peak at 81.6 ml consistent with a tetramer; and one at 87.6 ml corresponding to the dimer fraction. Pfc_His eluted as a single peak at 64 ml, which has a slightly larger apparent size than the decamer fraction of Rru_EncFtn (Fig. 1A). When subjected to SDS-PAGE the Hoch_His peak fractions were partially resistant to SDS and heat-induced denaturation, presenting bands at the approximate molecular weight of a monomer and dimer species (Fig. S4A); the Pfc_His peak fractions were almost fully resistant to SDS and heat denaturation with the majority of protein appearing as a band with an apparent molecular weight greater than that of a decamer, with a small proportion of monomer (Fig. S4B). Bands corresponding to dimer and monomer states were observed with Rru_His variant (Fig. S4C). The StrepII-tagged variants of the proteins behaved slightly differently in solution (Fig. 1B); Hoch_StrepII eluted as a monomer; while the Pfc_StrepII had a major decamer peak with two additional peaks consistent with higher-order aggregation, such as dimers of decamers and trimers of decamers. The Rru_StrepII protein eluted primarily as a decamer. Their appearance on SDS-PAGE gels was almost identical to the His-variants, with the appearance of some tetramer in the Pfc_StrepII fractions (Fig. S4D/E/F).

Native Mass spectrometry analysis

In order to further understand the differences seen in the solution-phase oligomerization states of the EncFtn homologues, native mass spectrometry was performed on the His-tagged variant of each homologue. As previously reported [1], the decameric assembly of iron-bound Rru_EncFtn can be successfully detected using this technique. Under native MS conditions (at pH 8.0), Rru_EncFtn displays a narrow charge state distribution consistent with the 22+ to 25+ charge state of the protein decamer (Fig. 2A, pink circles). In addition to the decamer, a minor species is observed which is consistent with the iron-free Rru_EncFtn monomer (+6 and +7) (Fig. 2A, blue circles).

In a similar manner to Rru_EncFtn, native MS analysis of Pfc_EncFtn demonstrates charge state distributions consistent with a decameric assembly (+23 to +26) (Fig. 2B, pink circles). Interestingly, the decameric charge state distribution is elongated (Fig. 2B, *) and low abundance (27+ to 31+) charge states are also observed. The elongated charge state distribution is only observed in Pfc_EncFtn, and we attribute its presence to the ability of the solvent-exposed affinity tag to readily protonate in solution. Similar to the observations from Rru_EncFtn, a charge state distribution

consistent with iron-free Pfc_EncFtn monomer (+5 to +17) is also observed (Fig. 2B, blue circles). In contrast, native MS analysis of Hoch_EncFtn does not reveal a major decamer species. Instead a series of oligomerization states are observed: the major species is a dimer (+9 to +12) (Fig. 2C, green circles); in addition tetramer (+13 to +16), hexamer (17+ and 18+) and decamer (23+ to 25+), and a small amount of monomer (+7 to +12) gas phase oligomerization states are all clearly observed (Fig. 2C, purple circles, orange circles, pink circles, and blue circles respectively). This observation is consistent with the multiple broad peaks obtained during size-exclusion chromatography (Fig. 1).

These data suggest that, under our experimental conditions, multiple oligomeric assemblies of Hoch protein exist in both the solution and gas phase. The observation of even-numbered oligomerization states (i.e. dimer, tetramer and hexamer) suggests that one of the two dimer interfaces is partially unstable, and the protein exists as an equilibrium of dimers and higher order multiples of dimers.

Crystal structures of Hoch and Pfc Encapsulated ferritins

To explore the structure of the EncFtn homologues, crystals of native Hoch_EncFtn and Pfc_EncFtn were produced by standard crystallization screening methods. Diffraction data were collected at Diamond Light Source and the crystal structures of the Hoch_EncFtn and Pfc_EncFtn proteins were determined by molecular replacement using a decamer of the Rru_EncFtn (PDB ID: 5DA5) as the search model [1]. Data collection and refinement statistics are shown in Table 1.

The structure of Hoch_EncFtn was refined at 2.06 Å resolution and contained a decamer in the asymmetric unit with visible electron density for residues 6 – 96 in each chain (Fig. 3A). Pfc_EnFtn was refined at 2.03 Å resolution and contained three decamers in the asymmetric unit, with visible electron density for residues 2-98 in each chain (Fig. 3B). The overall architecture of both structures mirrors the annular decamer seen in the structure of Rru_EncFtn (Fig. 3C). The electrostatic surfaces of these proteins display similar features to Rru_EncFtn, with negatively charged patches around the circumference that correspond to the exterior metal binding sites seen on Rru_EncFtn, and a negatively charged tunnel at the centre of the decamer corresponding to the interior metal binding site (Fig. S5).

277 The monomers of Hoch_EncFtn and Pfc_EncFtn superimpose with an RMSD of 1.21 Å over 74 Cα
278 atoms. Hoch_EncFtn superimposes on Rru_EncFtn with an RMSD of 0.47 Å over 91 Cα atoms,
279 while Pfc_EncFtn superimposes with an RMSD of 1 Å over 71 Cα atoms. While the Hoch_EncFtn
280 and Rru_EncFtn structures are almost identical, the Pfc_EncFtn structure presents several key
281 differences to these two proteins. At the N-terminus of Pfc_EncFtn, there is visible electron density
282 from Gly2, whereas the chains of both Hoch_EncFtn and Rru_EncFtn are not visible until residue
283 Gln6 and Ser7 respectively. The additional structured residues in Pfc_EncFtn form an extended loop
284 (Fig. 4), which lies in the central channel of the physiologically active decamer and forms a rigid
285 constriction when compared to the Hoch_EncFtn and Rru_EncFtn structures (Fig. 3B). The C-
286 terminal α3 helix of Pfc_EncFtn has two additional turns when compared to the other structures and
287 is shifted by 25° relative to α2 (Fig. 4B/C); this extends its interaction with the neighbouring dimer.
288 (Fig. 3B).

289 The main interaction surfaces that make up the decameric arrangement in the proteins correspond
290 to the ferroxidase centre dimer (FOC) and the non-ferroxidase dimer (non-FOC) interfaces (Fig.
291 3B/C). Analysis of the extent of these surfaces with PISA [25] gives a buried surface of 1186 Å^2 for
292 the Hoch_EncFtn FOC interface, with 8 hydrogen bonds and 16 salt bridges; and 1712 Å^2 in
293 Pfc_EncFtn, with 14 hydrogen bonds and 6 salt bridges (Fig S6). While Hoch_EncFtn buries roughly
294 the same surface area in its FOC interface as Rru_EncFtn FOC (1267 Å^2), the latter has only 2
295 hydrogen bonds and 6 salt bridges; the additional stabilization of this interface in Hoch_EncFtn is
296 likely related to the environmental niche of *Haliangium ochraceum*, as proteins from halophilic
297 organisms tend to have an increased number of salt bridges when compared to those from
298 mesophiles [26]. The Pfc_EncFtn FOC interface has fourteen hydrogen bonds and six salt bridges;
299 this significant increase in hydrogen bonding over the Rru_EncFtn protein is likely to be a
300 consequence of the hyperthermophilic nature of *Pyrococcus furiosus*. The non-FOC interface for
301 Hoch_EncFtn buries 2338 Å^2, which is similar to the 2468 Å^2 buried in this region in Rru_EncFtn;
302 however, there are 18 hydrogen bonds compared to 16 in Rru_EncFtn, and 5 salt bridges compared
303 to 16 in Rru_EncFtn. These differences are due to a higher proportion of buried hydrophobic residues
304 in the Hoch_EncFtn interface. The non-FOC interface in the Pfc_EncFtn is less extensive than either

of the other two structures at 1793 Å^{2,} with 19 hydrogen bonds and 19 salt bridges. The extended structured loop at the N-terminus and shifted α3 helix form one hydrogen bond each to the monomer next to their partner in the FOC interface, to bury an additional 586 Å^2 of surface area (Fig S6). Taken together, these two interfaces bury about the same surface area as the non-FOC interfaces of both Rru_EncFtn and Hoch_EncFtn. The extended interaction surfaces in the Pfc_EncFtn potentially act as a girdle around the decamer, further stabilizing it at high temperatures.

The residues in the iron binding site of the FOC interface are conserved in the Hoch_EncFtn and Pfc_EncFtn structures (Fig. 5). The Pfc_EncFtn structure shows clear anomalous difference density in data collected close to the iron edge at 1.74 Å (Fig. S7; therefore, a dinuclear iron centre was modelled into the FOC of this structure (Fig. 5). The metal coordination in Pfc_EncFtn is identical to that seen in Rru_EncFtn, with glutamic acid carboxyl oxygen to iron coordination distances of 2.1 Å, and histidine nitrogen to iron distances of 2.2 Å. The electron density in the FOC interface of the Hoch_EncFtn crystal does not contain any peaks or coordinated metal ions (Fig. S7). Given the importance of the histidine residue (His64) for iron coordination [1] and the fact that the protein crystallized in a buffer at pH 5.5, this histidine residue is likely to be around 70 % protonated and would be unable to coordinate iron in this state, thus explaining the absence of iron in this site. In the absence of iron in the Hoch_EncFtn structure, the side-chain of Glu31 is flipped 180° and is within hydrogen bonding distance of Tyr38 from the partner chain, presumably stabilizing the apo-form of this interface (Fig. 5A).

The secondary metal coordination sites seen in the structure of Rru_EncFtn are fully conserved in Hoch_EncFtn and only partially so in Pfc_EncFtn. The metal binding site at the centre of the decameric ring comprises Glu30/Glu33 in Hoch_EncFtn and Ala31/Asp34 in Pfc_EncFtn. Neither structure has any coordinated metal ions in this site (Fig. 5B).

The side-chains of the glutamic acid residues (Glu31/Glu34 in Rru_EncFtn numbering) are shifted when compared to those in Rru_EncFtn; this could be linked to the absence of a metal ion. The external metal binding site of Hoch_EncFtn is identical to the Rru_EncFtn site, while the Pfc_EncFtn has a glutamic acid in place of a histidine and alanine in place of a glutamic acid in this site.

Given the observation that a decameric form of Hoch_EncFtn was obtained in crystals at pH 5.5, the influence of pH on protein oligomerization was investigated using native MS. Experiments were performed in pH 5.5 ammonium acetate, and under these acidic conditions MS analysis reveals a substantial increase in the abundance of the decameric species (21+ to 25+) (Fig. S8), similar to the level seen for Pfc_EncFtn and Rru_EncFtn. The lower order oligomerization states, present at pH 8.0, are significantly reduced in abundance and only dimer (9+ and 10+) and tetramer (14+ and 15+) minor species are observed (Fig. S8, green and purple circles respectively). Taken together, our native MS observations suggest that a stable Hoch EncFtn dimer is readily formed irrespective of pH; and under acidic conditions, Hoch_EncFtn dimers favour assembly into the higher order pentamer-of-dimers annular structure which is characteristic of this class of protein.

Ferroxidase activity

Given the absolute conservation of the FOC residues in Hoch_EncFtn, Pfc_EncFtn and Rru_EncFtn, the ferroxidase activity of the EncFtn homologues was tested to determine if they were indeed active as ferroxidase enzymes. Encapsulated ferritin StrepII-tagged variants were assayed for their ferroxidase activity by following progress curves for iron oxidation at 315 nm at 20 °C. Each of the proteins displayed similar activity profiles, with some small differences in the shape of the progress curves. Hoch_EncFtn exhibits a higher initial rate than the other homologues (Fig. 6). Overall these data confirm the ferroxidase activity of the EncFtn family across different species from distinct environmental niches.

The metal content of the purified protein fractions used for enzymatic assays was determined by inductively coupled plasma mass spectrometry (Table S7). Iron levels determined in StrepII-tagged monomeric Hoch_EncFtn variants and StrepII-tagged decameric Pfc_EncFtn and Rru_EncFtn variants show an iron to protein ratio consistent with 40-80 % occupancy of the ferroxidase centre, assuming all of the iron is located within this site. A ~50 % occupancy of the ferroxidase centre was also observed with the His-tagged EncFtn variants which were used in the mass-spectrometry analysis.

Significant amounts of zinc were copurified with all protein samples in this study, with varying levels detected in the forms with different tags. Zinc is known to strongly inhibit the ferroxidase activity of

ferritin family proteins via competitive binding to the ferroxidase centre [27]. Given the structural differences between encapsulated ferritins and the classical ferritins, and the differences in secondary metal-binding sites displayed by Pfc_EncFtn, the inhibitory effect of zinc on the EncFtn homologues was tested by performing the ferroxidase assays in the presence of increasing concentrations of zinc. The results show that increasing zinc concentrations lead to a decrease in the slope and final level of ferroxidase progress curves for all of the EncFtn variants, with a maximum inhibition seen with ~ 40-100 μM Zn (Fig. S9). These data were fitted using a nonlinear regression with a dose-response model with three parameters, where the response (zero-subtracted end-point absorbance at 315 nm) was the average of three replicates per condition (Fig. 7). The calculated IC50 values for zinc inhibition of the three EncFtn variants (Table S8) show significant differences, with the Rru_EncFtn showing the lowest, and Hoch_EncFtn the highest IC_{50} values. The lower susceptibility of the Hoch_EncFtn to zinc dependent inhibition could be a consequence of a higher level of ferroxidase activity, or structural differences that influence metal binding and discrimination.

Discussion

The recently published structural and functional analysis of the *R. rubrum* encapsulated ferritin system presented a new functional organization for iron mineralization by ferritin-like proteins, with the four-helix bundle ferritin-like fold formed through the interaction of EncFtn subunits to form a functional ferroxidase centre [1]. The open decameric structure of the EncFtn protein is not competent to store iron in mineral form; instead, the interaction with, and sequestration within, the encapsulin nanocage provides a functional and high-capacity iron storage system [3,4]. To understand whether the structural organization of the EncFtn family is conserved across microorganisms with different environmental niches and distinct encapsulin geometries, we determined the structure and biochemical properties of EncFtn proteins from *H. ochraceum* and *P. furiosus*.

P. furiosus is a hyperthermophilic Euryarchaeota and its encapsulin was the first to be characterized; however, it was initially mis-annotated as a non-functional virus-like particle [13]. The *P. furiosus* encapsulin forms a contiguous polypeptide chain with an N-terminal EncFtn domain appended to it and assembles into a 180 subunit T=3 capsid. This archaeal arrangement is distinct to the bacterial EncFtn/encapsulin systems, which are usually encoded in a two-gene operon with the EncFtn upstream of the encapsulin, and with a short C-terminal encapsulation sequence peptide appended to the encoded EncFtn protein [5,10]. It is not clear whether the genomic arrangement of the bacterial EncFtn/encapsulin systems arose separately, or by horizontal gene transfer from archaea followed by mutation of the single-reading frame into two, along with the mutation of the T=3 form of the encapsulin to the T=1 form found in the bacterial EncFtn encapsulins.

The published crystal structure of the *P. furiosus* encapsulin lacks any electron density for the EncFtn domain, implying that this domain is mobile within the encapsulin nanocage even though it is contiguous with and tethered to the encapsulin protein [13]. Our analysis focused on the isolated *P. furiosus* EncFtn domain, which forms a decamer in solution, the gas phase, and in crystals. This domain is partially resistant to thermal and SDS induced denaturation, which is in accord with the extreme temperatures endured by the host organism in its volcanic niche.

The current model for the organization of bacterial EncFtn proteins within encapsulin nanocages places the decamers at the pentameric vertices of the T=1 capsid [1,4] with the encapsulation sequences of five subunits captured by clefts on the interior surface of the penton of the encapsulin shell. The encapsulation sequences of the other five subunits in the decamer are disengaged and free within the interior of the capsid. No evidence is available on the strength of the interaction between the capsid and the EncFtn protein; however, the presence of clear electron density for some of the encapsulation sequence in the *T. maritima* encapsulin structure implies that the interaction is relatively stable, and this is enhanced by an avidity mechanism with multiple encapsulation sequences engaged by subunits at the pentameric vertex [4]. In the archaeal systems the EncFtn and encapsulin domains are a contiguous polypeptide, with the EncFtn domain tethered to the interior of the capsid. The T=3 geometry of the *P. furiosus* encapsulin has 180 subunits, with 12 penton units and 20 hexons. Given the structural and biochemical conservation of the decameric EncFtn protein, it is likely that this arrangement is found within the T=3 as well as T=1 capsids. It is not clear how the decamer could be formed from tethered subunits unless the EncFtn domains found in hexons have enough flexibility in the linker between domains to engage with partners in adjacent pentons. With full engagement at the pentons, this would leave 60 ‘free’ EncFtn domains within the capsid. This observation, coupled with our solution and gas phase experiments, indicates that the quaternary structure of EncFtn proteins is dynamic and that they can exist in equilibrium between monomers/dimers and higher order multiples of dimers.

The dynamic nature of EncFtn proteins is highlighted in our solution and gas phase analyses of the *H. ochraceum* EncFtn. Despite high sequence identity and the conservation of key residues between it and the *R. rubrum* EncFtn, this protein is less prone to multimerization in solution and displays a greater range of oligomerization intermediates than both the *R. rubrum* and *P. furiosus* EncFtn proteins in the gas phase. The presence of the conserved EncFtn decamer quaternary structure in the crystal highlights the conservation of this architecture. The absence of metal ions in the crystal structure, which was formed at pH 5.5, indicated that the quaternary structure can be induced by both metal binding, as was shown in solution for the *R. rubrum* EncFtn [1], and changes in pH, presumably through the protonation of the conserved histidine at low pH and the formation of stabilizing hydrogen bonds by residues normally involved in the formation of the FOC.

Analysis of the structure and sequence of the *H. ochraceum* EncFtn indicates that the dimerization interfaces are less extensive than the *R. rubrum* EncFtn interfaces and are discontinuous. This leads to lower binding energies for both of the interfaces when compared to both *R. rubrum* and *P. furiosus,* and this could explain the differences in stability seen in solution and the gas phase.

We show here that the three proteins in this study exhibit comparable ferroxidase activities. This indicates that they were purified in a functional state. Previous reports show that ferritins are susceptible to inhibition by Zn(II) ions [27], which is also the case for the EncFtn family as demonstrated in this study. In the experimental conditions used in our study, the *H. ochraceum* EncFtn was slightly more active than the other proteins and less susceptible to inhibition by zinc. This may be a consequence of the more dynamic nature of this homologue, as seen in solution and the gas phase. The precise mode of catalysis for ferritins is a subject of some debate and key questions as to whether the iron ions engaged within the ferroxidase centre are labile, or act as a stable prosthetic centre; and whether the two iron ions move in concert are the subject of some controversies in the field [28,29]. Our study does not aim to address these controversies, but we do note that the location of the conserved FOC and secondary metal binding sites at a dimer interface and the dynamic nature of EncFtn oligomerization may indicate a distinct mechanism of iron oxidation and transfer to minerals when compared to the classical ferritins, thus adding a new level of complexity and debate to the field. It must also be noted that the activity of EncFtn proteins occurs within the privileged environment of an encapsulin shell, which adds an additional level of complexity to the study of their catalysis.

Analysis of the sequence alignment (Fig. S3) highlights the absence of conserved residues found in the putative metal ion entry site found in the other EncFtn homologues. Our observation that Pfc EncFtn displays ferroxidase activity highlights that conservation of this site is not a prerequisite for catalysis. However, it is clear that Pfc_EncFtn has the lowest enzymatic activity of the three homologues, it may be that that the acidic residues found in this location attract iron ions and channel them to the FOC. Their absence in Pfc_EncFtn implies that metal ions reach its FOC simply by diffusion, resulting in a slower Fe(II)/Fe(III) turn-over and hence a reduction in enzyme activity. It would be interesting to apply a mutagenesis approach to further explore the role of these proposed

461 entry site residues on the ferroxidase activity. The modest catalytic activity displayed by Pfc_EncFtn
462 could also be interpreted by considering that *P. furiosus* achieves optimal growth at ~ 100 °C,
463 whereas enzymatic experiments were conducted at room temperature to allow the comparison of
464 activities.

465 Further study will shed light on the role of the different dimerization interfaces on the stability of the
466 EncFtn decamer; and the role of the secondary metal binding sites on catalysis, metal selectivity,
467 and catalytic inhibition by competing metal ions.

468

Author Contributions

DH, JMW and DC conceived the study. DH produced the native and His-tagged constructs used in the study. LRT produced the DNA parts and assembled the StrepII-tagged variants of the EncFtn proteins. DH, CP, JR, ZM and JMW produced recombinant proteins used in the study. DH and JMW determined and refined the crystal structures. CP performed biochemical assays shown in Figures 6/7/S9. JR and DC performed mass spectrometry experiments shown in Figures 2 and S8. CLM provided technical assistance and contributed to data collection for MS experiments. KJW and ET performed ICP-MS experiments shown in Table S7. All authors contributed to data analysis and preparation of the manuscript.

Funding

This work was supported a Royal Society Research Grant awarded to JMW (RG130585) and a BBSRC New Investigator Grant to JMW and DJC (BB/N005570/1). JMW is funded by Newcastle University. DJC and JR are funded by the University of Edinburgh. JR is funded by a BBSRC EastBio DTP studentship (BB/M010996/1). DH was funded by the China Scholarship Council. LRT was funded by a BBSRC EastBio DTP Studentship (BB/M010996/1). KJW and ET were funded by the Wellcome Trust and Royal Society through a Sir Henry Dale Fellowship awarded to KJW (098375/Z/12/Z).

Competing Interests

The authors declare that there are no competing interests.

Acknowledgements

The authors would like to thank Diamond Light Source for beamtime (proposal mx9487), and the staff of beamlines I04 and I24 for assistance with crystal testing and data collection.

We would like to thank Prof Dominic Campopiano and Dr Elisabeth Lowe for their critical reading of this manuscript and helpful discussions.

References

1 He, D., Hughes, S., Vanden-Hehir, S., Georgiev, A., Altenbach, K., Tarrant, E., Mackay, C. L. L., Waldron, K. J. K. J., Clarke, D. J. D. J. and Marles-Wright, J. (2016) Structural characterization of encapsulated ferritin provides insight into iron storage in bacterial nanocompartments. Elife **5**, e18972.

2 Andrews, S. C. (2010) The Ferritin-like superfamily: Evolution of the biological iron storeman from a rubrerythrin-like ancestor. Biochim. Biophys. Acta, Elsevier B.V. **1800**, 691–705.

3 McHugh, C. A., Fontana, J., Nemecek, D., Cheng, N., Aksyuk, A. A., Heymann, J. B., Winkler, D. C., Lam, A. S., Wall, J. S., Steven, A. C., et al. (2014) A virus capsid‐like nanocompartment that stores iron and protects bacteria from oxidative stress. EMBO J., EMBO Press **33**, 1896–1911.

4 Sutter, M., Boehringer, D., Gutmann, S., Günther, S., Prangishvili, D., Loessner, M. J., Stetter, K. O., Weber-Ban, E. and Ban, N. (2008) Structural basis of enzyme encapsulation into a bacterial nanocompartment. Nat. Struct. Mol. Biol., Nature Publishing Group **15**, 939–947.

5 Giessen, T. W. and Silver, P. A. (2017) Widespread distribution of encapsulin nanocompartments reveals functional diversity. Nat. Microbiol., Nature Publishing Group **2**, 17029.

6 Crow, A., Lawson, T. L., Lewin, A., Moore, G. R. and Le Brun, N. E. (2009) Structural basis for iron mineralization by bacterioferritin. J. Am. Chem. Soc., American Chemical Society **131**, 6808–13.

7 Bakker, G. R. and Boyer, R. F. (1986) Iron incorporation into apoferritin. The role of apoferritin as a ferroxidase. J. Biol. Chem. **261**, 13182–13185.

8 Bradley, J. M., Moore, G. R. and Le Brun, N. E. (2014) Mechanisms of iron mineralization in ferritins: one size does not fit all. J. Biol. Inorg. Chem. **19**, 775–85.

9 Chasteen, N. D. and Harrison, P. M. (1999) Mineralization in ferritin: an efficient means of iron storage. J. Struct. Biol. **126**, 182–94.

10 Sutter, M., Boehringer, D., Gutmann, S., Günther, S., Prangishvili, D., Loessner, M. J., Stetter,

K. O., Weber-Ban, E. and Ban, N. (2008) Structural basis of enzyme encapsulation into a bacterial nanocompartment. Nat. Struct. Mol. Biol. **15**, 939–947.

11 Snijder, J., Kononova, O., Barbu, I. M., Uetrecht, C., Rurup, W. F., Burnley, R. J., Koay, M. S. T., Cornelissen, J. J. L. M., Roos, W. H., Barsegov, V., et al. (2016) Assembly and Mechanical Properties of the Cargo-Free and Cargo-Loaded Bacterial Nanocompartment Encapsulin. Biomacromolecules **17**, 2522–9.

12 Rurup, W. F., Snijder, J., Koay, M. S. T., Heck, A. J. R. and Cornelissen, J. J. L. M. (2014) Self-sorting of foreign proteins in a bacterial nanocompartment. J. Am. Chem. Soc., American Chemical Society **136**, 3828–32.

13 Akita, F., Chong, K. T., Tanaka, H., Yamashita, E., Miyazaki, N., Nakaishi, Y., Suzuki, M., Namba, K., Ono, Y., Tsukihara, T., et al. (2007) The crystal structure of a virus-like particle from the hyperthermophilic archaeon Pyrococcus furiosus provides insight into the evolution of viruses. J. Mol. Biol. **368**, 1469–83.

14 Iverson, S. V., Haddock, T. L., Beal, J. and Densmore, D. M. (2016) CIDAR MoClo: Improved MoClo Assembly Standard and New E. coli Part Library Enable Rapid Combinatorial Design for Synthetic and Traditional Biology. ACS Synth. Biol., American Chemical Society **5**, 99–103.

15 Kabsch, W. (2010) Integration, scaling, space-group assignment and post-refinement. Acta Crystallogr. Sect. D Biol. Crystallogr., International Union of Crystallography **66**, 133–144.

16 Evans, P. R. (2011) An introduction to data reduction: space-group determination, scaling and intensity statistics. Acta Crystallogr. D. Biol. Crystallogr. **67**, 282–92.

17 Evans, P. (2006) Scaling and assessment of data quality. In Acta Crystallographica Section D: Biological Crystallography, pp 72–82, International Union of Crystallography.

18 Stein, N. (2008) CHAINSAW: A program for mutating pdb files used as templates in molecular replacement. J. Appl. Crystallogr. **41**, 641–643.

19 Terwilliger, T. C., Grosse-Kunstleve, R. W., Afonine, P. V., Moriarty, N. W., Zwart, P. H., Hung, L. W., Read, R. J. and Adams, P. D. (2007) Iterative model building, structure refinement and

density modification with the PHENIX AutoBuild wizard. Acta Crystallogr. Sect. D Biol. Crystallogr., International Union of Crystallography **64**, 61–69.

20 Afonine, P. V., Grosse-Kunstleve, R. W., Echols, N., Headd, J. J., Moriarty, N. W., Mustyakimov, M., Terwilliger, T. C., Urzhumtsev, A., Zwart, P. H. and Adams, P. D. (2012) Towards automated crystallographic structure refinement with phenix.refine. Acta Crystallogr. Sect. D Biol. Crystallogr., International Union of Crystallography **68**, 352–367.

21 Emsley, P., Lohkamp, B., Scott, W. G. and Cowtan, K. (2010) Features and development of Coot. Acta Crystallogr. D. Biol. Crystallogr. **66**, 486–501.

22 Chen, V. B., Arendall, W. B., Headd, J. J., Keedy, D. A., Immormino, R. M., Kapral, G. J., Murray, L. W., Richardson, J. S. and Richardson, D. C. (2010) MolProbity: all-atom structure validation for macromolecular crystallography. Acta Crystallogr. D. Biol. Crystallogr. **66**, 12–21.

23 Sievers, F. and Higgins, D. G. (2014) Clustal Omega, accurate alignment of very large numbers of sequences. Methods Mol. Biol. **1079**, 105–16.

24 Gouet, P., Robert, X. and Courcelle, E. (2003) ESPript/ENDscript: Extracting and rendering sequence and 3D information from atomic structures of proteins. Nucleic Acids Res. **31**, 3320–3.

25 Krissinel, E. and Henrick, K. (2007) Inference of macromolecular assemblies from crystalline state. J. Mol. Biol. **372**, 774–97.

26 DasSarma, S. and DasSarma, P. (2015) Halophiles and their enzymes: negativity put to good use. Curr. Opin. Microbiol. **25**, 120–126.

27 Pfaffen, S., Abdulqadir, R., Le Brun, N. E. and Murphy, M. E. P. (2013) Mechanism of ferrous iron binding and oxidation by ferritin from a pennate diatom. J. Biol. Chem. **288**, 14917–25.

28 Ebrahimi, K., Eckhard, B., Hagedoorn, P. and Hagen, W. (2012) The catalytic center of ferritin regulates iron storage via Fe (II)-Fe (III) displacement. Nat. Chem. Biol. **8**, 941–948.

29 Hagen, W. R., Hagedoorn, P.-L. and Honarmand Ebrahimi, K. (2017) The workings of ferritin:

575 a crossroad of opinions. Metallomics, The Royal Society of Chemistry **9**, 595–605.

576

577

Tables

Table 1. X-ray diffraction data collection and refinement statistics.

	Hoch_EncFtn	Pfc_EncFtn*
Data collection		
Wavelength (Å)	1.72	1.74
Resolution range (Å)	47.82 - 2.06 (2.13 - 2.06)	47.19 - 2.03 (2.1 - 2.03)
Space group	C 1 2 1	P 1 21 1
Unit cell (Å) **β (°)**	91.63, 92.65, 119.29 106.94	99.85, 110.06, 136.27 91.22
Total reflections	30,0549 (27,242)	1,226,338 (112,156)
Unique reflections	57,293 (5,570)	374,905 (36,076)
Multiplicity	5.2 (4.9)	3.3 (3.0)
Completeness (%)	96.3 (94.1)	97.0 (95.4)
Mean I/sigma(I)	10.16 (2.37)	10.48 (4.02)
Wilson B-factor (Å^2)	31.7	22.8
R_{merge} (%)	9.4 (59.6)	8.0 (36.3)
R_{meas} (%)	10.5 (66.7)	9.5 (44.1)
R_{pim} (%)	4.4 (29.2)	5.2 (24.7)
$CC_{1/2}$ (%)	100 (99.9)	99.5 (90.2)
CC* (%)	100 (97.6)	100 (97.4)
Image DOI	10.5281/zenodo.322743	10.5281/zenodo.344797
Refinement		
Reflections used in refinement	57,082 (5,563)	365,581 (36,036)
Reflections used for R-free	2,765 (284)	17,934 (1697)
Rwork (%)	20.1 (29.5)	17.5 (22.3)
Rfree (%)	24.5 (34.5)	20.2 (24.5)
CC(work) (%)	96.4 (92.6)	96.7 (92.3)
CC(free) (%)	93.6 (85.1)	95.3 (90.3)
Non-hydrogen atoms	7,819	25,735
macromolecules	7,650	23,691
ligands	1	30
Water	168	2,014
Protein residues	916	2,922
RMS(bonds) (Å)	0.003	0.002
RMS(angles) (°)	0.46	0.44
Ramachandran		
favoured (%)	98.7	99.9
allowed (%)	1.3	0.10
outliers (%)	0.00	0.00
Rotamer outliers (%)	0.96	0.39
Clashscore	1.20	1.15
Average B-factor (Å2)	44.6	29.0
macromolecules	44.6	28.3
ligands	34.7	19.7
solvent	43.7	36.7
PDB ID	5N5F	5N5E

*Anomalous pairs were counted separately for Pfc_EncFtn, as this model was refined against the split anomalous data. Statistics for the highest-resolution shell are shown in parentheses.

583 **Figures**

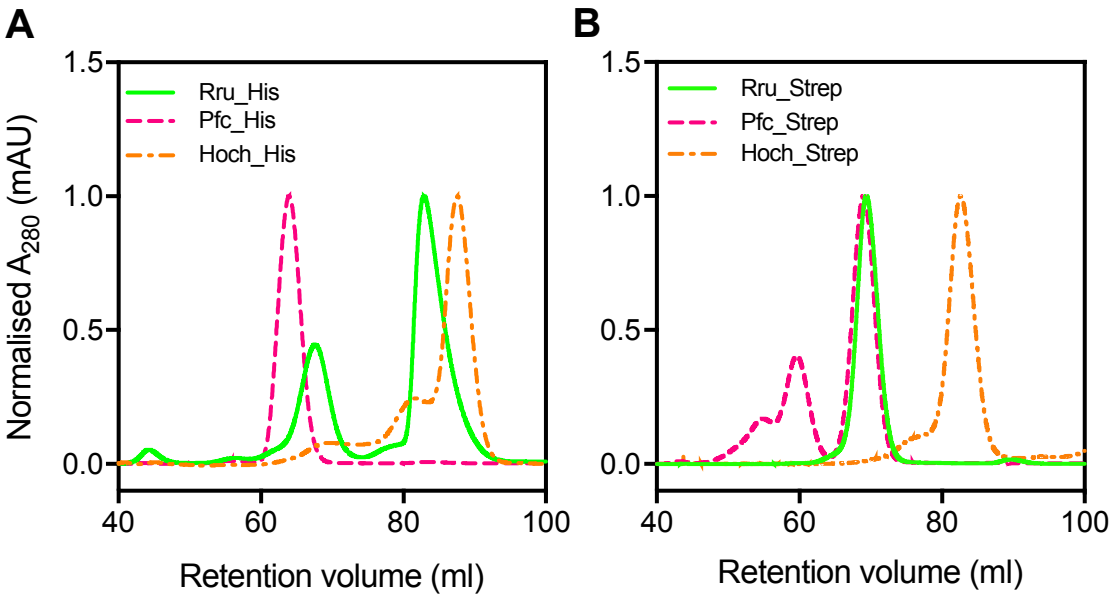

584

585 **Figure 1. Purification of recombinant *R. rubrum*, *H. ochraceum*, and *P. furiosus* EncFtn**
586 **proteins.** *A*, Recombinant His-tagged Hoch_His, Pfc_His, and Rru_His proteins were purified by
587 nickel NTA-affinity chromatography and subjected to analytical size-exclusion chromatography
588 using a Superdex 200 16/60 column (GE Healthcare) equilibrated with 50 mM Tris-HCl, pH 8.0,
589 150 mM NaCl. The peaks near 70 ml correspond to an estimated molecular weight of >130 kDa
590 when compared to calibration standards, consistent with oligomerisation states equal or greater
591 than decameric. The Hoch_His at around 80 ml corresponds to the 50 kDa tetramer and the peaks
592 near 88 ml correspond to the 31 kDa dimer compared to the standards. *B*, Recombinant Strep-
593 tagged Hoch_StrepII, Pfc_StrepII, and Rru_StrepII proteins were purified by Strep-Trap column HP
594 (GE Healthcare). Purified samples were applied to a Superdex 200 16/60 column (GE Healthcare)
595 equilibrated with 50 mM Tris-HCl, pH 8.0, 150 mM NaCl in order to observe oligomerization state
596 in solution. Rru_StrepII elutes primarily at ~ 70 ml, corresponding to the decamer size. Pfc_StrepII
597 peaks can be found around 60 ml (~ 24-mer) and at 70 ml (12-mer), whereas Hoch_StrepII elutes
598 at ~ 83 ml (4-mer). Elution volumes and corresponding oligomerisation states are summarised in
599 Table S6. DOI: 10.6084/m9.figshare.7105907

600

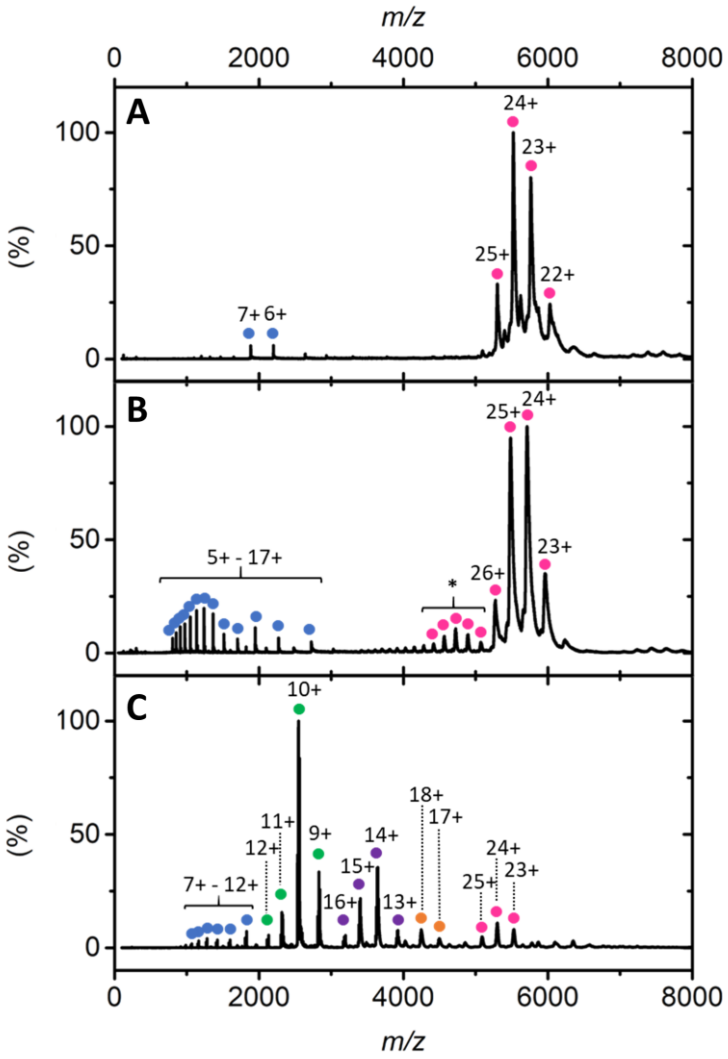

Figure 2. Native mass spectrometry of encapsulated ferritin homologues. Native nanoelectrospray ionization (nESI) mass spectrometry of encapsulated ferritin homologues acquired in 100 mM ammonium acetate (pH 8.0). *A*: nESI spectrum of Rru_EncFtn consistent with decameric assembly. The decameric charge state distribution is represented with pink circles and peaks correspond to 22+ to 25+ charge states. Two minor monomer charge states (blue circles, 6+ and 7+ charge states) are also observed. *B:* Native spectrum of Pfc_EncFtn. Decamer charge states (23+ to 31+) are highlighted with pink circles and monomer charge states (5+ to 17+) are highlighted by blue circles. * denotes the extended charge state observed. *C:* nESI spectrum of Hoch_EncFtn with gas phase oligomerization stressed with coloured circles. Monomer shown as blue; dimer as green; tetramer as purple; hexamer as yellow and decamer as pink.

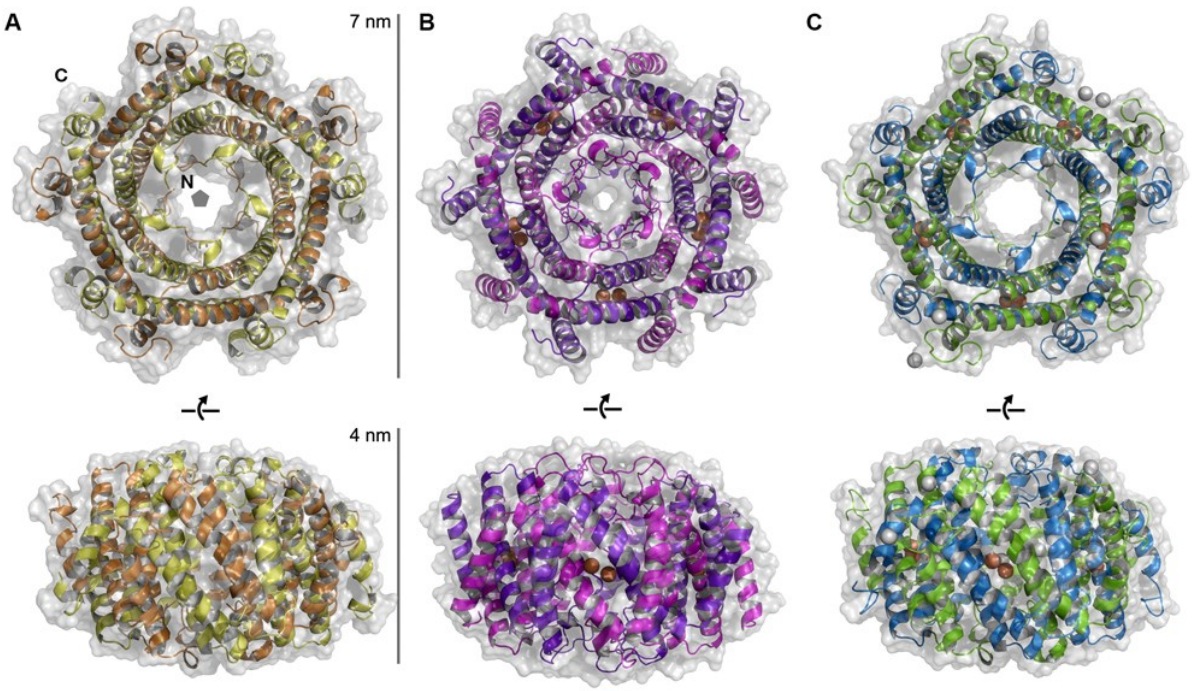

Figure 3. Encapsulated ferritins from *Haliangium ochraceum* and *Pyrococcus furiosus* form annular decamers. The annular decameric architecture of the encapsulated ferritins from *Haliangium ochraceum, A*, and *Pyrococcus furiosus, B*, are shown as transparent solvent accessible surfaces over secondary structure cartoons. The published structure of the *Rhodospirillum rubrum* encapsulated ferritin is shown for comparison, *C* (PDB ID: 5DA5) [1]. Bound metal ions are shown as spheres: iron ions are depicted in orange, and calcium ions in grey. The positions of the N- and C-termini of the protein chains and five-fold symmetry axis are highlighted in panel *A*.

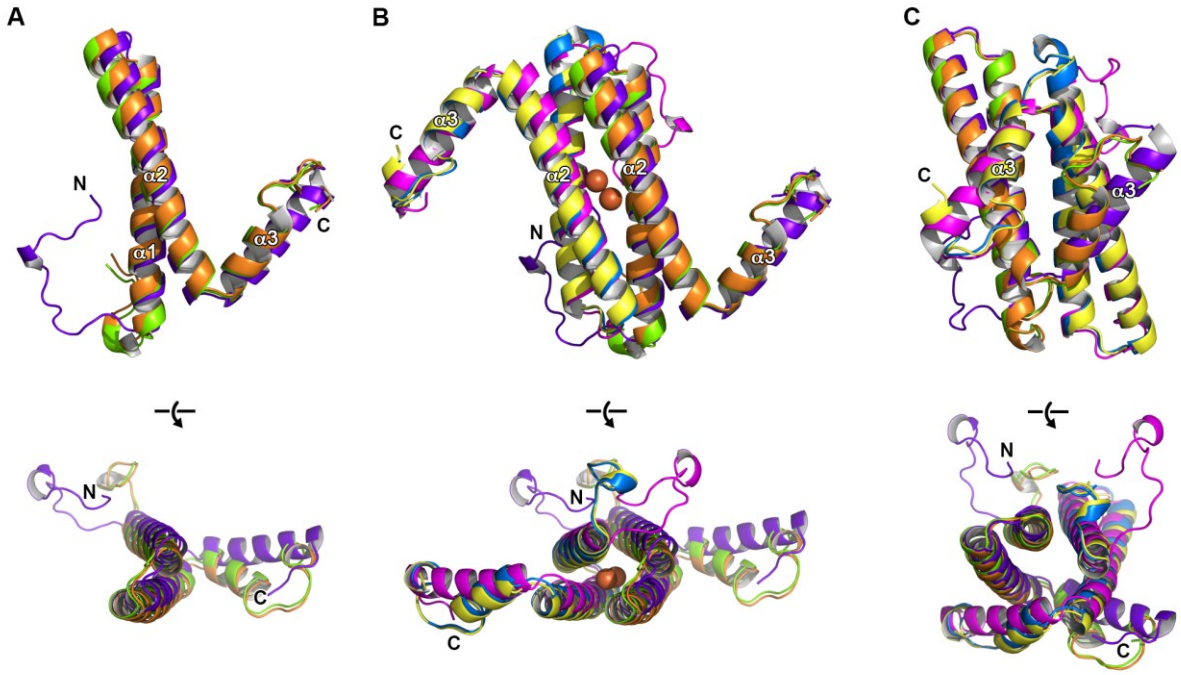

Figure 4. Crystal structures of encapsulated ferritins from *Haliangium ochraceum* and *Pyrococcus furiosus.* Secondary structure cartoon depictions of the structures of the protomers and dimers found in the crystal structures of the Hoch_EncFtn and Pfc_EncFtn encapsulated ferritins. *A*, orthogonal views of the protomers: Hoch_EncFtn shown in orange; Pfc_EncFtn in purple; and Rru_EncFtn in green for comparison (PDB ID: 5DA5) [1]. *B*, orthogonal views of the ferroxidase centre dimer. Iron ions present in the Pfc_EncFtn dimer are shown as orange spheres. No metal ions were present in the Hoch_EncFtn structure. Hoch_EncFtn is shown in orange/yellow; Pfc_EncFtn in purple/pink; and Rru_EncFtn in green/blue. *C*, orthogonal views of the non-FOC dimer, depicted as in *B*.

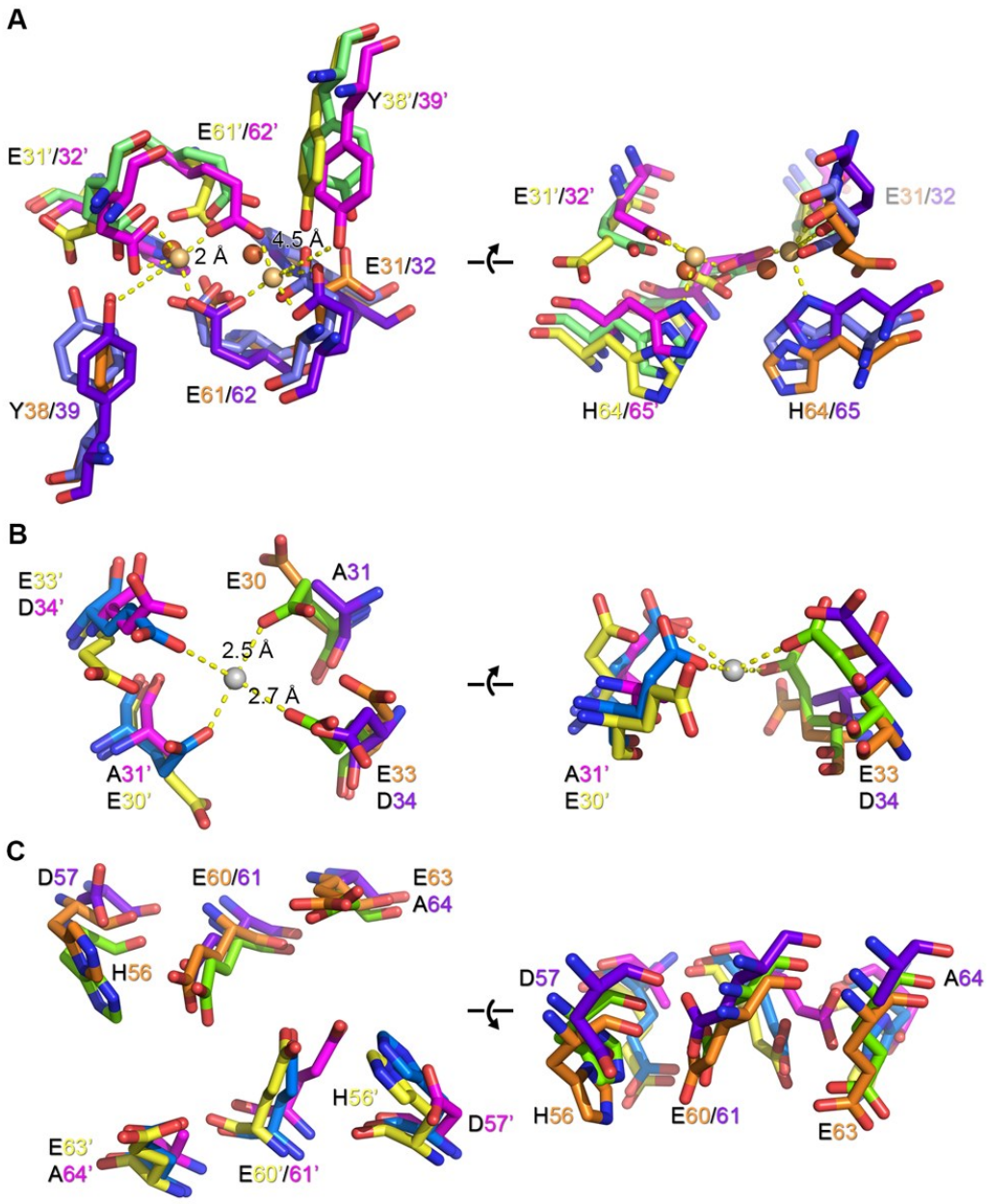

Figure 5. Ferroxidase centre and putative metal binding sites of encapsulated ferritins. Orthogonal views of the ferroxidase centre (*A*) and putative secondary metal binding sites (*B/C*) of Hoch_EncFtn (yellow/orange) and Pfc_EncFtn (pink/purple) compared to Rru_EncFtn (PDB ID: 5DA5) [1] (blue/green). *A*, conserved ferroxidase centre residues are numbered for Hoch_EncFtn and Pfc_EncFtn. Iron ions found in the Pfc_EncFtn FOC are shown as gold spheres with coordination distances to side chain atoms shown. The positions of the iron ions in the Rru_EncFtn structure are shown as orange spheres. *B*, residue conservation in the site occupied by calcium in the Rru_EncFtn structure (grey sphere, with coordination distances). *C,* conserved residues on the outer surface of the encapsulated ferritin surface, located 10 Å from the FOC.

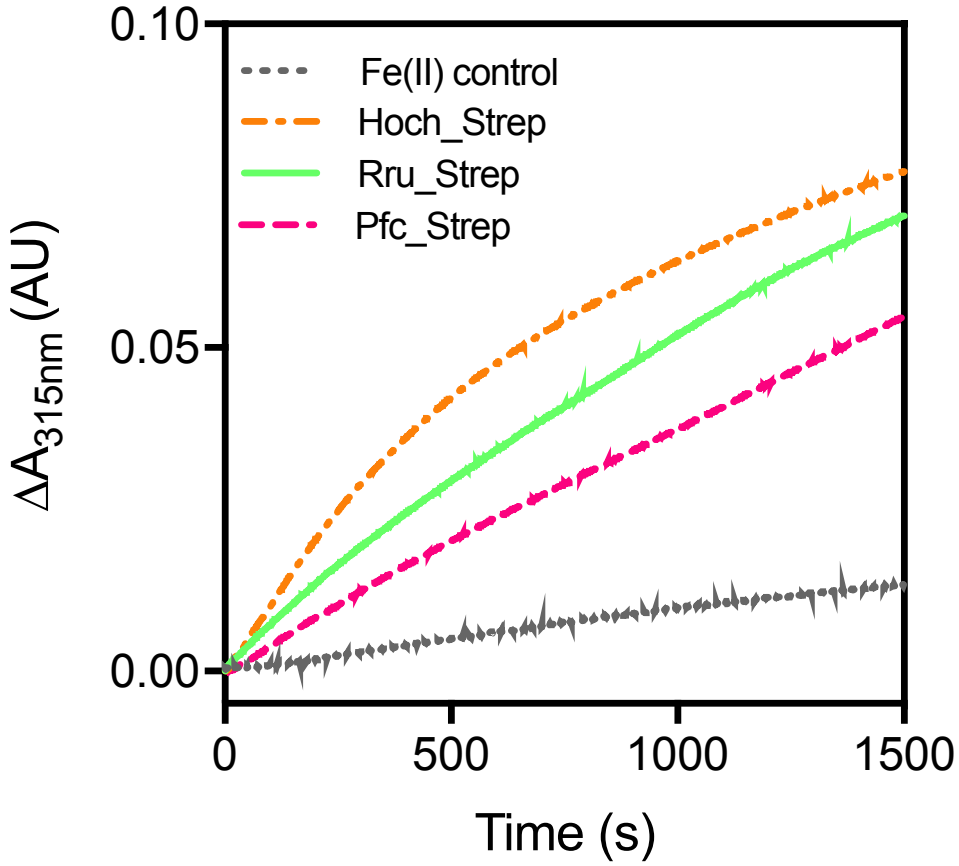

644

645 **Figure 6. Ferroxidase activity of encapsulated ferritins.** Hoch_StrepII(dotdash orange line),
646 Pfc_StrepII(dashed pink line), and Rru_StrepII(solid green line) (10 μM monomer) were incubated
647 with 50 μM $FeSO_4.7H_2O$ (10 times molar equivalent Fe^{2+} per FOC) and progress curves of the
648 oxidation of Fe^{2+} to Fe^{3+} was monitored at 315 nm. The background oxidation of iron at 50 μM in
649 enzyme-free control is shown for reference (dotted grey line). Solid lines represent the average (n
650 = 3) of technical replicates, shaded areas represent standard deviation from the mean.
651 DOI: 10.6084/m9.figshare.7718879
652

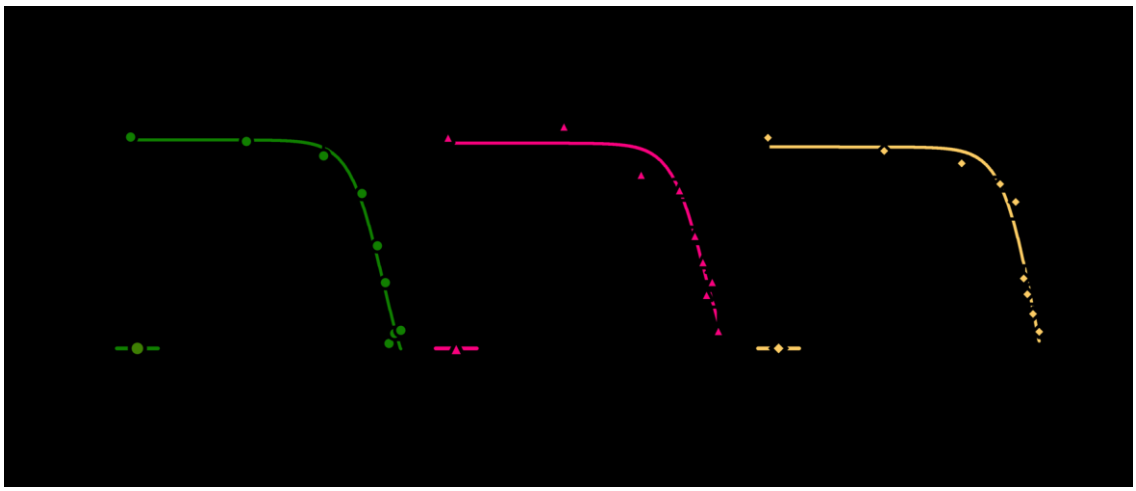

Figure 7. The ferroxidase activity of encapsulated ferritins is inhibited by zinc. *A, B, C,* Non-linear fit of ferroxidase activities of Strep-tagged proteins inhibited by varying concentrations of Zn(II) by GraphPad software using a Dose-Response (log(inhibitor) vs. response (three parameters) equation. Response used in this analysis is the average of three technical replicates per condition. Data shown were recorded after 1500 seconds from the start of the assay. IC_{50} and $logIC_{50}$ have been calculated for each protein (Table S8). DOI: 10.6084/m9.figshare.7718879